Book Title
Book Editors
IOS Press, 2003

Needle Artifact Localization in 3T MR Images [1]

S.P. DiMaio [a,2], D.F. Kacher [a], R.E. Ellis [a], G. Fichtinger [b], N. Hata [a], G.P. Zientara [a], L.P. Panych [a], R. Kikinis [a], F.A. Jolesz [a]

[a] *Brigham and Women's Hospital, Harvard Medical School*
[b] *Johns Hopkins University*

Abstract. This work explores an image-based approach for localizing needles during MRI-guided interventions, for the purpose of tracking and navigation. Susceptibility artifacts for several needles of varying thickness were imaged, in phantoms, using a 3 tesla MRI system, under a variety of conditions. The relationship between the true needle positions and the locations of artifacts within the images, determined both by manual and automatic segmentation methods, have been quantified and are presented here.

Keywords. needle tracking, magnetic resonance imaging, susceptibility artifact

1. Introduction

This study explores the feasibility of localizing standard MRI-compatible needles by detecting their susceptibility artifacts directly from images, for the purpose of tracking and navigation during MRI-guided interventions. A variety of approaches for tracking instruments in MRI have been presented in the past [1–4]. Although typically fast and accurate, such approaches can have drawbacks such as line-of-sight limitations, heating, sensitive tuning, calibration and expense. Passive tracking approaches, in which the needle position is detected directly from the images, provide an alternative solution. Paramagnetic needles produce field distortions that appear as local regions of signal loss [5] when imaged. The advantages of an image-based passive tracking approach are that needles and devices do not require expensive instrumentation, and that both the interventional device and the patient's anatomy are observed together in the same image space. There is, however, a compromise between imaging speed and quality that can degrade needle localization accuracy and reliability. The visual appearance of susceptibility artifacts produced by needles in 0.2, 0.5, 1.0 and 1.5 Tesla MRI images has been

[1]This work was partially funded by NSF ERC 9731748, NIH 5-P01-CA067165-07 and 1-U41-RR019703.

[2]Correspondence to: Simon DiMaio, Brigham and Women's Hospital, 75 Francis Street, Boston, 02115. E-mail: simond@bwh.harvard.edu

characterized in [6–9], while techniques for optimizing visualization of artifacts are described in [10].

The paper is organized as follows: Section 2 describes a set of needle artifact imaging experiments performed in a 3T MRI system, as well as the methods used to localize and compare needle and needle artifact positions computed from images. Section 3 presents a summary of results quantifying the location of needle artifact in the images. Finally, Section 4 concludes with an interpretation of the results and scope for future work.

2. Materials and Methods

We localized needles by automatically detecting image artifacts using fast imaging sequences that are useful for interventional guidance and navigation. Three needles of varying thickness (18G×10cm, 20G×10cm and 22G×10cm MRI histology needles, E-Z-EM Inc.) were clamped horizontally in an acrylic needle holder, as shown in Figures 1(a) and (b). The needle holder was attached to the bottom of a plastic container, but was free to rotate in the horizontal plane, with gradations marked at 10° intervals for accurate orientation. For imaging, we used

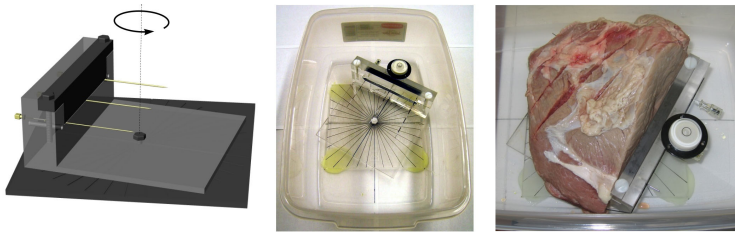

(a) (b) (c)

Figure 1. Experiment apparatus: (a,b) rotating acrylic needle holder, (c) needles embedded in an ex vivo tissue sample.

a 3-tesla MRI scanner (GE Healthcare, Milwaukee, WI). The plastic container was placed into a standard head imaging coil (GE quadrature birdcage) and filled with a Nickel Chloride solution (< 1% NiCl). The needle holder included two cylindrical fiducials precisely machined in the same plane as the needles, for scan plane alignment, and to determine the true needle positions within the images. All combinations of the imaging protocols, needle orientations, image orientations and phase/frequency-encoding directions, listed below, were imaged.

Imaging Protocol:	*Single-Shot Fast Spin Echo* (SSFSE) and *Fast Gradient Recalled Echo* (FGRE).
Needle Orientation:	Needle axis horizontal, $0 - 90°$ with respect to B_0 in 10° increments.
Slice Orientation:	Single image with needles in plane, and a set of images taken transversely through the needle shafts, from base to tip (to be called axial images).
Frequency Direction:	Parallel and perpendicular to the needle shaft for in-plane images.

Standard half-Fourier single-shot fast spin echo (SSFSE) and fast gradient recalled echo (FGRE) imaging protocols were used: **2D SSFSE** (TR=2500ms, TE=65.832ms, flip angle=90°, 62.5kHz bandwidth, 24cm FOV, 0.9375 pixel spac-

ing, 4mm slice, 256×256 matrix, 0.5 NEX); **2D FGRE** (TR=29ms, TE= 5.5ms, flip angle=30°, 15.63kHz bandwidth, 24cm FOV, 0.9375 pixel spacing, 4mm slice, 256×128 matrix, 1 NEX). Scan time per image was less than four seconds for the SSFSE and less than one second for the FGRE.

The experiments were repeated with the needles inserted into an ex vivo tissue sample, as shown in Figure 1(c). Needles were rotated axially while being inserted into the tissue, and symmetrical bevels were used to minimize needle deflection.

2.1. Artifact Detection

In this preliminary study, we used a primitive artifact-detection algorithm to illustrate the feasibility of image-based needle localization. Each in-plane needle image was processed in order to determine: 1) the true needle positions, 2) the centroid and tip of each artifact by manual segmentation, and 3) the automatically detected centroid and tip of each artifact. The true needle positions were determined by detecting the needle holder fiducials which have a known relationship to the needles. Each image is divided into three regions of interest, each containing just one needle artifact. Automatic detection of each artifact is computed using an algorithm based on the linear Hough transform, as shown in Figure 2. The detection algorithm operates on both the raw image regions and their

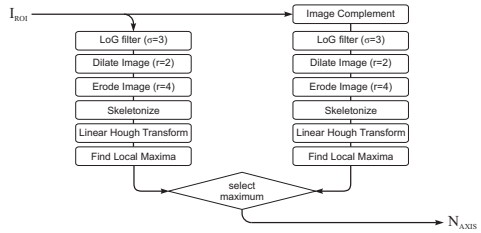

Figure 2. Flowchart illustrating the artifact detection algorithm.

complements (grayscale intensities inverted), in order to detect both enhancing and non-enhancing needle artifacts. Occasional manual intervention was required to correct a poor decision in the final step of the algorithm; otherwise, all other parameters remained constant for all images. The tip of each artifact was computed by finding the peak image intensity gradient along the detected artifact axis N_{AXIS}.

3. Results

Examples of needle artifacts are shown in Figure 3. The FGRE artifacts are significantly larger than the SSFSE artifacts when perpendicular to B_0. Artifacts are shifted along the frequency-encoding direction in both SSFSE and FGRE sequences, and become better defined when this direction is perpendicular to the needle shaft. The quantitative relationship between the artifact location and true needle position is illustrated in Figure 4, where both the difference in tip depths and shaft positions are shown. Here, the artifact location is based on a manual

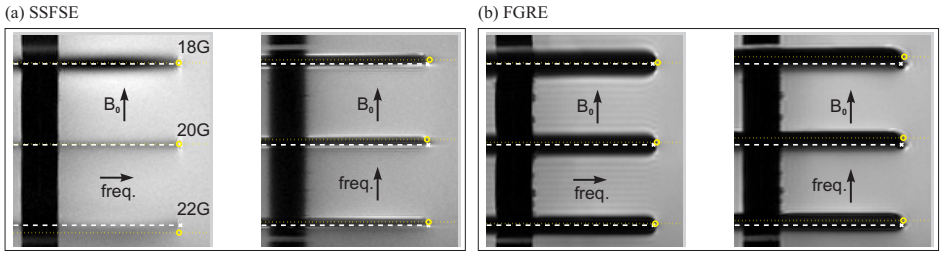

Figure 3. Artifacts with needles perpendicular to B_0, imaged with (a) SSFSE, and (b) FGRE, with needles emersed in a NiCl solution. Frequency-encoding directions both parallel and perpendicular to the needle shaft are shown. Dashed lines and crosses are actual needle shaft and tip, while dotted lines and circles indicate detected artifact.

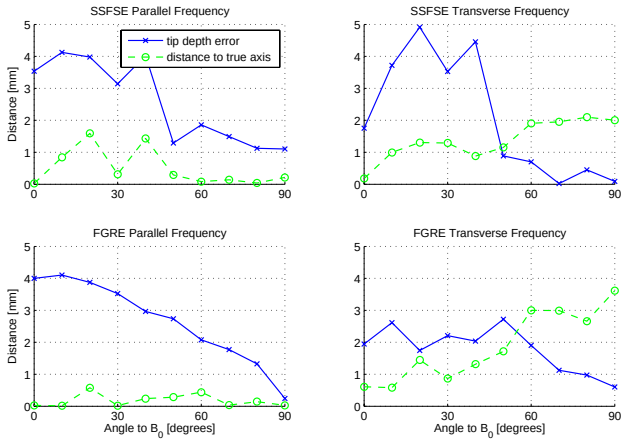

Figure 4. Comparison of manually segmented artifact to true needle position. Results for the 20G needle are shown.

segmentation for which the centroid and tip of the artifact were determined visually. When the needle is parallel to B_0, the visible SSFSE artifacts tend to under-represent the tip depth by up to 5mm and the FGRE artifacts tend to over-represent the tip depth by up to 4mm; however, these discrepancies decrease to below 1mm by the time the needle is perpendicular. The centroid of the artifact is very close to the true needle axis (<1mm) when the frequency-encoding direction runs parallel to the needle; however, when the frequency direction is perpendicular, the artifact is increasingly shifted away from the needle axis as the needle is rotated to 90° from B_0. For SSFSE images, this shift reaches 2mm, while the FGRE images exhibit a maximum shift of 3.6mm—this is visible in Figure 3. These results are shown for the 20G needle, while similar behaviour is observed for the 18G and 22G needles.

The automatic artifact detection algorithm was compared against both the true needle position and the manually segmented artifact location. In Figure 5 the distance between the detected artifact axis, and the true axis, evaluated at the needle tip, is plotted with respect to the needle orientation angle. The distance to the manually specified artifact centroid is also shown. For all combinations of the

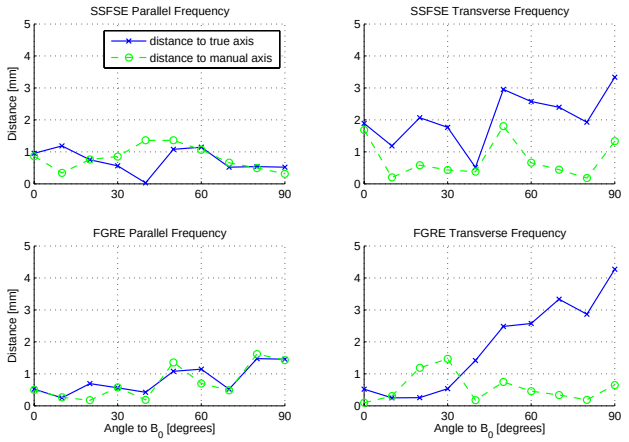

Figure 5. Comparison of automatically segmented artifact to true needle positions and manually segmented artifact. Results for the 20G needle are shown.

imaging sequence and frequency-encoding direction, the automatically detected artifact axis lies well within 2mm of the visible artifact (manually segmented artifact centroid). However, when the frequency-encoding direction is perpendicular to the needle, the detected artifact is shifted with respect to the true needle, increasing with B_0 angle. In the SSFSE and FGRE images, this shift reaches 3.4mm and 4.4mm, respectively, in a manner similar to that observed in Figure 4. Similar results were obtained for 18G and 22G needles. Transverse images of the needle shafts exhibit similar characteristics as in-plane images. Artifact size and shift increase with B_0 angle, particularly when using the FGRE sequence. All of the abovementioned imaging was repeated using an ex vivo tissue sample. Similar needle detection results were obtained from these images, as shown in Figure 6.

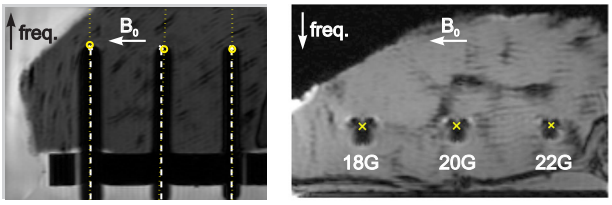

(a) (b)

Figure 6. Needle artifact in a tissue sample: (a) in-plane images indicating true needle (dashed line and cross) and detected artifact (dotted line and circle); (b) axial image with true needle axes marked.

4. Conclusions

Artifact characteristics appear to vary systematically with respect to the B0 angle and frequency-encoding direction, which implies three opportunities for future work. First, from knowledge of these critical parameters, it may be possible to

correct for the spatial shifts of the artifacts from a single image; this might be possible with a combination of a physics-based approach (e.g., based on dipole field models) and empirically determined corrections. Second, multiple orthogonal images may be useful in correcting for the spatial shift. Finally, from the angle of the artifact with respect to the B0 and frequency-encoding directions, it may be possible to optimize the frequency direction from image to image and to adapt echo time and bandwidth to perform real-time control of the MRI sequences to optimally image a needle during an interventional procedure.

This work is significant because robust and reliable needle and device tracking will be required for tracking and navigation of needle placement inside the 3T magnet bore, using either manual or robot-assisted positioning. A localization approach that does not rely upon additional instrumentation, and that is intrinsically registered to the targeting plan is highly desirable. This study indicates the feasibility of such an approach.

References

[1] S. G. Silverman, B. D. Collick, M. R. Figueira, R. Khorasani, D. F. Adams, R. W. Newman, G. P. Topulos, and F. A. Jolesz, "Interactive MR-guided biopsy in an open-configuration MR imaging system," in *Radiology*, vol. 197(1), pp. 175–181, 1995.

[2] C. L. Dumoulin, S. P. Souza, and R. D. Darrow, "Real-time position monitoring of invasive devices using magnetic resonance," in *Magnetic Resonance in Medicine*, vol. 29, pp. 411–415, 1993.

[3] J. A. Derbyshire, G. A. Wright, R. M. Henkelman, and R. S. Hinks, "Dynamic scan-plane tracking using MRI position monitoring," in *J. Mag. Res. Imag.*, vol. 8(4), pp. 924–932, 1998.

[4] S. G. Hushek, B. Fetics, R. M. Moser, N. F. Hoerter, L. J. Russell, A. Roth, D. Polenur, and E. Nevo, "Initial Clinical Experience with a Passive Electromagnetic 3D Locator System," in *5^th Interventional MRI Symp., Boston MA*, pp. 73–74, 2004.

[5] J. F. Schenck, "The role of magnetic susceptibility in magnetic resonance imaging: MRI magnetic compatibility of the first and second kinds," in *Medical Physics*, vol. 23(6), pp. 815–850, 1996.

[6] C. Frahm, H. Gehl, U. H. Melchert, and H. Weiss, "Visualization of Magnetic Resonance-Compatible Needles at 1.5 and 0.2 Tesla," in *Cardiovascular Interventional Radiology*, vol. 19, pp. 335–340, 1996.

[7] M. E. Ladd, P. Erhart, J. F. Debatin, B. J. Romanowski, P. Boesiger, and G. C. McKinnon, "Biopsy Needle Susceptibility Artifacts," in *Magnetic Resonance in Medicine*, vol. 36, pp. 646–651, 1996.

[8] J. S. Lewin, J. L. Duerk, V. R. Jain, C. A. Petersilge, C. P. Chao, and J. R. Haaga, "Needle Localization in MR-Guided Biopsy and Aspiration," in *American Journal of Radiology*, vol. 166, pp. 1337–1345, 1996.

[9] H. J. Langen, H. Kugel, W. Heindel, T. Krahe, J. Gieseke, and K. Lackner, "Localization of puncture needles in MRI: experimental studies on precision using spin-echo sequences at 1.0 T," in *Rofo Fortschr Geb Rontgenstr Neuen Bildgeb Verfahr*, vol. 167(5), pp. 501–508, 1997.

[10] K. Butts, J. M. Pauly, B. Daniel, S. Kee, and A. Norbash, "Management of Biopsy Needle Artifacts: Techniques for RF-Refocused MRI," in *Magnetic Resonance Imaging*, vol. 9, pp. 586–595, 1999.